



ELSEVIER

Contents lists available at ScienceDirect

Cold Regions Science and Technology

journal homepage: www.elsevier.com/locate/coldregions

Metrics for interpreting the microstructure of sea ice using X-ray micro-computed tomography



R.M. Lieb-Lappen*, E.J. Golden, R.W. Obbard

Dartmouth College, Thayer School of Engineering, 14 Engineering Drive, Hanover, NH, United States

ARTICLE INFO

Article history:

Received 3 November 2015

Received in revised form 20 February 2017

Accepted 4 March 2017

Available online 8 March 2017

Keywords:

X-ray micro-computed tomography

Sea ice

Brine channel microstructure

ABSTRACT

As the character and dynamics of sea ice change in a rapidly changing climate, it is critical to have a detailed understanding of the fine microstructure of sea ice. Advances in X-ray micro-computed tomography (μ CT) technology have enabled non-destructive three dimensional analysis of the brine channel morphology with resolution down to several microns. In this study, we examine six ice cores collected from the Ross Sea, Antarctica. Metrics were developed to describe the shape, size, and topology of the brine channels and air pockets in sea ice. A cubic sub-sample measuring 6.0 mm on edge was found to be the representative elementary volume for sea ice μ CT analysis with these metrics. All samples were observed to have vertically oriented cylindrical brine channels, with increased branching and connectivity observed at lower depths. The highest degree of vertical anisotropy was detected through the middle, with increased variability near the top and bottom of each core. Air pockets were found to be mostly spherical in shape, except vertically elongated in multi-year ice.

© 2017 The Authors. Published by Elsevier B.V. This is an open access article under the CC BY license (<http://creativecommons.org/licenses/by/4.0/>).

1. Introduction

The use of X-ray micro-computed tomography (μ CT) has exploded over the last decade due to rapid advances in instrumentation technology and accessibility through commercially available benchtop μ CT systems (Ketcham and Carlson, 2001; Stock, 2008). The primary advantage of μ CT is that it provides a non-destructive three-dimensional visualization and characterization of the internal features of multiphase and porous materials with spatial resolution down to several microns. Once the phases of a given material have been segmented, the analysis of the μ CT data then produces quantitative measurements on topology and structure of the material. This has natural applications for describing microstructure mathematically and modeling microstructure-dependent properties of different porous media in fields varying from sedimentary rock and sea ice (e.g., Golden et al., 2007; Obbard et al., 2009) in the geosciences to bone analysis in biology (e.g., Campbell et al., 2007) to engineered composite materials (Naik et al., 2006).

μ CT utilizes the fact that phases of different density have varying absorption and transmission of X-ray radiation. Through the photoelectric effect, heavier elements are significantly more absorbing of X-rays than lighter elements, allowing separate phases to be

differentiated (Ketcham and Carlson, 2001). Since sea ice consists primarily of three phases (ice, brine, and air) with quite different densities, it is well suited for μ CT structural analysis.

Prior to the introduction of μ CT analysis, microstructural study of sea ice was limited to either destructive techniques or indirect measurements on a particular property of the ice (Weeks and Ackley, 1982). This presents challenges for highly detailed characterization of both air and brine inclusions, which vary both spatially and temporally with the thermal evolution of the sea ice. Brine inclusions are of primary importance because they provide critical pathways for the exchange of heat, gases, salts, and other chemical species, affecting processes such as nutrient delivery to microorganisms (e.g., Krembs et al., 2011), snow photochemistry (e.g., Grannas et al., 2007), salinity profile evolution (e.g., Cox and Weeks, 1975), and melt pond formation (Polashenski et al., 2012). Early work utilized thin section optical microscopy and found brine inclusions to be more elongated than air pockets (Light et al., 2003; Perovich and Gow, 1996). Cole and Shapiro (1998) further characterized the brine channel network, quantifying size and aspect ratios over time, and noting that in addition to the large vertically oriented channels, there are a number of side branches. Weissenberger et al. (1992) found similar results using a freeze-casting technique in combination with scanning electron microscopy, and recorded increased branching in granular ice relative to columnar ice. Finally, Eicken et al. (2000) achieved similar inclusion statistics analyzing sea ice microstructure with nuclear magnetic resonance imaging, and examined the thermal evolution of

* Corresponding author.

E-mail address: ross.lieb-lappen@vtc.vsc.edu (R.M. Lieb-Lappen).

the fluid inclusions. All of these techniques however, are highly constrained by stereological and resolution artifacts when quantifying the fine-scale morphology of the brine network (Eicken et al., 2000).

The use of cooling stages has permitted μ CT to be used to study the pore structure of cryospheric samples such as snow (e.g., (Wang and Baker, 2013; Wålin et al., 2014)), firn (e.g., Freitag et al., 2004; Schneebeli and Sokratov, 2004; Gregory et al., 2014) and ice cream (Pinzer et al., 2012). Pringle et al. (2009) analyzed CsCl-doped laboratory-grown sea ice and observed changes in brine channel connectivity at varying temperatures. Results supported percolation-theory predictions of critical anisotropic connectivity thresholds (Golden et al., 2007; Pringle et al., 2009). More recently, methods which involved analyzing field-collected sea ice have been developed (Maus et al., 2009, 2013; Obbard et al., 2009). Maus et al. (2009) developed methods using synchrotron μ CT by first centrifuging samples and storing at sub-eutectic temperatures. Although this protocol could not distinguish between closed, brine-filled pores and ice, the open porosity was removed of liquid and thus, less-likely to be altered during storage and transport (Maus et al., 2009). Further work with this method provided insight into pore size distribution, permeability, and applications to modeling oil entrapment, although no critical percolation threshold was observed (Maus et al., 2013).

The purpose of this study is to establish a robust methodology for analyzing sea ice microstructure using μ CT and introduce metrics for quantifying its morphology. The considerations, protocols, and metrics presented here however, can be adapted to the μ CT study of any porous media. To demonstrate the capabilities of this methodology, we examine the microstructure of natural first-year and multi-year sea ice cores that were used in two companion papers (Lieb-Lappen and Obbard, 2015; Obbard et al., 2016). Reactive bromine species play a large role in tropospheric ozone depletion events, and Lieb-Lappen and Obbard (2015) examines the role of the blowing snow in the activation of bromine over first-year Antarctic sea ice. The brine channels in the sea ice are critical in providing a transport mechanism for the salts to reach the sea ice surface. The precise locations for the first-year ice cores were chosen to maximize the contact of blowing snow with the ice surface, while the multi-year ice core was used for comparison purposes. Obbard et al. (2016) analyzes the microstructural location of particular salts within the sea ice cores. Here we use μ CT to study the microstructure of the sea ice cores and the transport processes through the brine channels, whereby linking the location of the salts (Obbard et al., 2016) to the photochemistry on the sea ice surface (Lieb-Lappen and Obbard, 2015).

In Section 2 of this manuscript we will describe the sample preparation and μ CT methodology. We will then introduce the metrics used for microstructural quantification in Section 3. In Section 4, we will present our results from the six ice cores analyzed, providing detailed microstructural descriptions for each phase segmented (brine, air, and ice). Additionally, we will present our results from both a spatial variability and temperature sensitivity analysis, as well as our calculation of the representative elementary volume required for this analysis. In Section 5, we will discuss the physical significance of our results and conclude the manuscript in Section 6.

2. Methods

2.1. Sample preparation

Sea ice cores were collected in October–November 2012 from six different locations in the Ross Sea, Antarctica, as shown in Fig. 1. The first two sites, named Butter Point and Iceberg Site, were located on first-year ice about 5 km from the open ocean at distances of 35 km and 55 km from the Ross Ice Shelf, respectively. The measured thickness of the ice at these two locations were 1.78 m and 1.89 m, respectively. The next three sites were also on first-year ice and

located on a transect at distances of 6, 12, and 18 km southeast from the ice edge, with thicknesses of 1.70, 1.80, and 1.82 m, respectively. To compare the microstructure of first-year sea ice to multi-year ice, an additional ice core measuring 1.96 m in length was extracted 700 m off-shore from Scott Base, Ross Island. Immediately following each core extraction, we recorded the temperature profile at 10-cm intervals, and stored the cores in a -20°C freezer at McMurdo station prior to shipping. All sea ice cores were transported at a constant temperature of -20°C back to Thayer School of Engineering's Ice Research Laboratory at Dartmouth College with temperature monitored with data loggers and stored in a -33°C cold room. μ CT analysis was then completed on cubic sub-samples measuring 1.5 cm on edge that were extracted every 10 cm along the length of each ice core. Minimal brine drainage was observed during core extraction as the brine volume fraction is relatively low in early Austral spring, and no brine drainage was observed during μ CT processing 6–12 months later.

Vertical thin sections of each core were cut and imaged using cross-polarizing lenses. The frazil ice fractions were 7.8%, 15.9%, 45.0%, 8.2%, 33.9%, and 21.9% for the Butter Point, Iceberg Site, Scott Base, and the three transect cores (6 km, 12 km, and 18 km), respectively. The columnar ice fractions were 28.3%, 56.6%, 26.2%, 30.0%, 22.6%, and 19.7%, respectively and the platelet ice fractions were 63.9%, 27.5%, 28.7%, 61.8%, 43.5%, and 58.5%, respectively. A more thorough description of the relative percentages of different ice types in each core is provided in the companion paper to this manuscript (Obbard et al., 2016).

2.2. Scanning

The components of a μ CT system are an X-ray source, sample stage, a scintillator, and a photo detector. For this work, we used a Skyscan 1172 μ CT scanner that uses a sealed microfocus X-ray tube with a spot size of $5\ \mu\text{m}$ to produce a fixed conical, polychromatic X-ray source. In order to choose the accelerating voltage for the X-ray source, it is helpful to know the expected absorption of the specimen, and ensure minimum transmission does not drop below 20%. For 30 kV X-rays, the mass attenuation coefficient for water/ice is $0.3756\ \text{cm}^2/\text{g}$, while for 40 kV X-rays it is $0.2683\ \text{cm}^2/\text{g}$ (Hubbell and Seltzer, 1995). Since sea ice has an approximate density of $900\ \text{kg}/\text{m}^3$ (Hutchings et al., 2015; Timco and Frederking, 1996), this leads to linear attenuation coefficients of $\mu = 33.804\ \text{m}^{-1}$ and $\mu = 24.147\ \text{m}^{-1}$ for 30 kV and 40 kV X-rays, respectively. The resulting X-ray transmission is expressed by the Beer-Lambert law:

$$I = I_0 e^{-\mu x} \quad (1)$$

where I_0 is the initial beam intensity, μ is the linear attenuation coefficient, and x is the distance traveled through the specimen. Since $x \approx 0.015\ \text{m}$ for all samples, roughly 40% of the X-ray signal is attenuated for 30 kV X-rays and 30% of the X-ray signal is attenuated for 40 kV X-rays. Ice cores collected from Butter Point, Iceberg Site, and Scott Base were scanned at an accelerating voltage of 30 kV and a current of $100\ \mu\text{A}$. By increasing the accelerating voltage to 40 kV with a current of $250\ \mu\text{A}$ for samples from the transect cores, we were able to reduce acquisition time, while maintaining adequate contrast. A test sample was run at both settings, and by implementing appropriate segmentation as discussed below, we showed that differences between the two scanning setups were negligible.

Each sample was frozen onto a Peltier thermoelectric cooling stage that could maintain temperature at -20°C . Each sample was then rotated 180° about its vertical axis in 0.7° steps, and the transmitted X-rays were imaged at each step. The geometry and spot size of the X-ray source determines the acquisition time required and the spatial resolution of the scan (Landis and Keane, 2010). For the setup

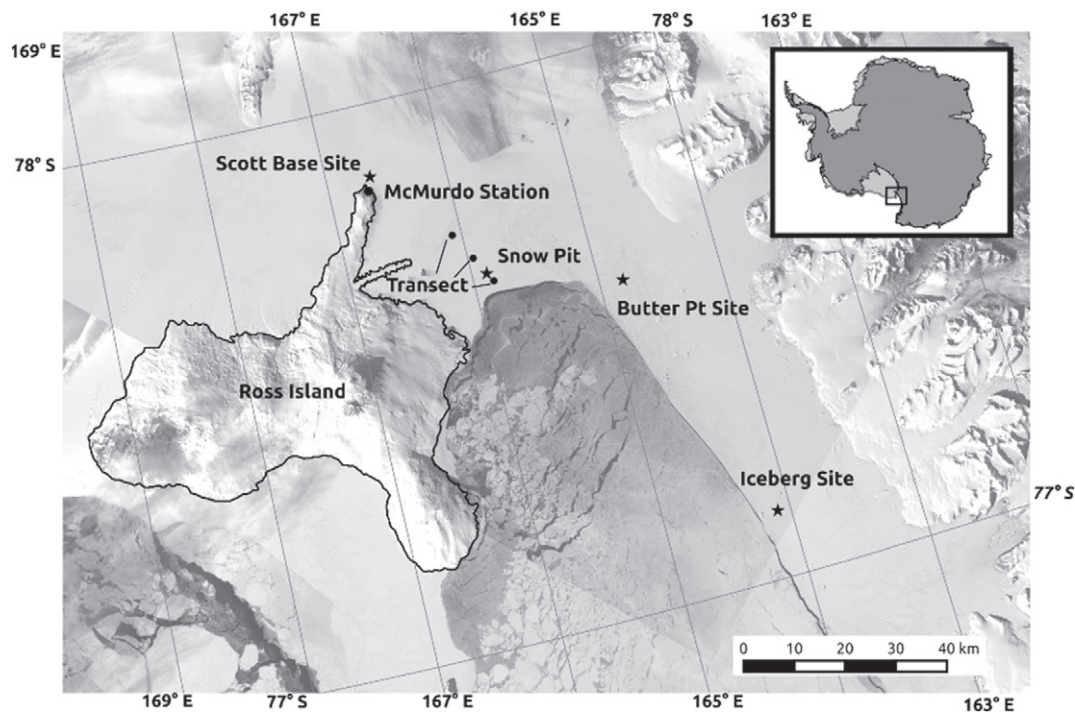


Fig. 1. Map of the Ross Sea region showing all of the field sites used in this study. Basemap is Landsat image.

used in this work, the resulting scan time was approximately 20 min and the spatial resolution was 15 μm .

The final step of the scanning process is detecting the X-rays that pass through the specimen after each rotational step. The X-rays strike a scintillator screen that converts the X-rays into visible light photons that are then detected by a camera (Landis and Keane, 2010). Our Skyscan 1172 scanner utilizes a 1.3 Mp (1280 \times 1024) cooled Hamamatsu CCD camera fiber-optically coupled to the scintillator. For each rotation step, a single projection radiograph is produced with 4096 (12-bit) brightness graduations. Each day, prior to using the scanner, it is critical to normalize the detector by collecting a flat field image, where the detector observes the response of a uniform dark and white signal. The exposure time is adjusted to ensure that the beam intensity is 50–70% without the flat field correction. When scanning at 30 kV the exposure time was 2662 ms, while at 40 kV the exposure time was reduced to 847 ms.

2.3. Reconstruction

The next step of the μCT process is tomographic reconstruction of the projection radiographs into two-dimensional gray-scale slices stacked in the z -direction. First, the dark-field image acquired with no X-rays present is subtracted from each projection radiograph. Then, each radiograph is divided by the white-field or “flat-field” image, which is acquired with the X-rays on but no specimen present. For a given rotation angle, the radiographs represent a line integral of the X-ray photons not attenuated. Skyscan’s NRECON reconstruction software was used to solve the inverted Radon transform, which transforms the X-ray projections using a modified Feldkamp cone-beam algorithm to produce a stack of gray-scale cross-section images. During the reconstruction step, each voxel is assigned a value on an arbitrary scale known as CT values or Hounsfield Units (HU). A correspondence to linear attenuation coefficients and density can be made by using a calibrated scale with water equal to 0 HU and air equal to -1000 HU (Ketcham and Carlson, 2001). For all samples in this study, linear attenuation coefficient

endpoints of 0 to 0.07 were chosen to encompass the range of HU/CT values encountered, thereby enabling the conversion of each voxel into a standard 0–255 gray-scale.

μCT analysis is limited by anything that reduces the ability to set proper and consistent thresholds during segmentation. Thermal drift of the X-ray source during imaging, one such factor, was corrected by taking several extra projection radiographs spaced 45° apart. These post-analysis images are then compared to the original radiographs to determine the degree of thermal drift. Ring artifacts arise in the gray-scale image as a result of shifts in the output of individual detectors (Ketcham and Carlson, 2001). These shifts are often due to factors such as changes in temperature or beam strength, and result in anomalous values occurring in a ring centered on the rotational axis because the artifact affects each projection image. Ring artifacts were removed in the image post-processing by subtracting out the anomalous values for the compromised detector prior to reconstruction. Beam hardening is the most common artifact in images, and is the result of low energy X-rays preferentially being attenuated as they pass through the specimen (Ketcham and Carlson, 2001). Thus, the mean X-ray energy observed at the center of the specimen is greater than that observed near the edges. This results in the middle appearing darker than expected and edges appearing brighter. Since the degree of beam hardening was relatively small for this work, the post-processing corrections described above were sufficient, and the use of filters during imaging was not necessary.

Voxels that represent partial volumes of different phases present challenges during thresholding as a voxel is generally assigned to a single phase. The observed gray-scale value represents an average of the phases present. Regardless of the resolution of the μCT , partial volume effects will lead to a blurring of boundaries to some degree (Ketcham and Carlson, 2001). To reduce some of the noise in an image and help with boundary effects, pixels were smoothed based upon neighboring pixels using a Gaussian kernel.

Once image post-processing was completed, a interior cubic volume of interest (VOI) measuring 7.5 mm on each edge was selected from the center of the scanned volume. Morphometric analysis on

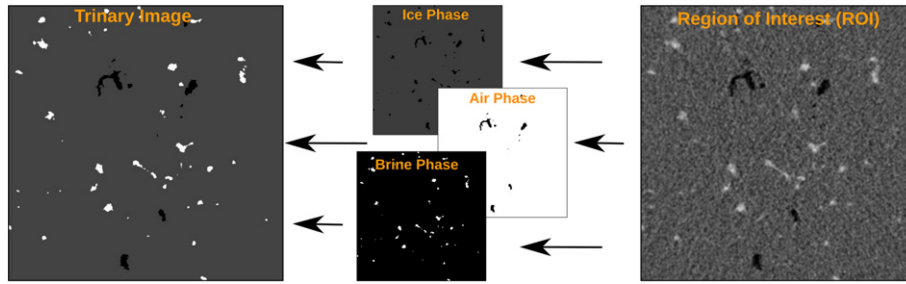


Fig. 2. Thresholding a trinary image of sea ice, where in the final trinary image, black represents air, white represents brine, and gray represents ice. First, a region of interest (shown on the right) is selected. A high threshold is set to pull out a binary image of only the brine phase. Next, a low threshold is set to pull out only the air phase. The in-between gray-scale values are used to pull out a binarized ice phase. The three binary images are then combined to create the trinary image shown on the left

the VOI was completed using Skyscan’s CTAn software package. By defining an interior VOI, we avoid microstructural damage on the edges caused by sample preparation.

The critical step in the entire μ CT process is thresholding the gray-scale images to set the boundaries of individual phases, since this dictates all subsequent qualitative and quantitative measurements. Because sea ice is a three-phase media, the desired output is a trinary image with separate thresholds for ice, brine, and air. Trinary images are often best segmented through the use of multiple binary images as is shown in Fig. 2. If enhanced contrast is required for segmentation, trinary images can be improved by doping a phase with an ion containing a strong absorption edge, as has been done using KI in soil systems (Costanza-Robinson et al., 2008) and CsCl in laboratory-grown sea ice (Golden et al., 2007; Pringle et al., 2009). In this technique, duplicate scans are done using X-ray energies above and below the absorption edge. This technique is best used with a synchrotron radiation source where monochromatic radiation and highly tunable X-ray energies are available. It was not required for proper segmentation of images here as the high resolution we used allowed for sufficient contrast of all three phases. As will be shown below, sufficiently high resolution leads to a reduction in mixed pixel values, thereby increasing the separation of each material’s peak in the histogram of gray-scale values.

Slight adjustments to the critical threshold values for a given phase can lead to significant differences in measured microstructural quantities. For example, Tarquis et al. (2009) used four different threshold values on a binary image to analyze the fractal dimension of soils, and noticed that although general trends did not change, measured values for porosity and fractal dimension varied significantly with the threshold level set (Tarquis et al., 2009). Thresholding can either be done manually by the user or through automated algorithms. Manual thresholding requires that the user compare binarized and gray-scale images thoroughly until a proper threshold value is set. Naturally, this method is subject to user bias and variability between different studies.

A variety of automated thresholding algorithms exist to remove the human element (e.g., clustering-based methods, the Otsu method, entropy-based methods, spatial methods examining neighboring voxels, inverse methods incorporating multiple thresholds) (Batenburg and Sijbers, 2009; Baveye et al., 2010). Wälén et al. (2014) segmented trinary images of NaCl-doped compacted snow by ensuring the measured brine volume matched the known amount of solution added. For this study, we successfully utilized a histogram shape-based approach that sets thresholds by examining the histogram of gray-scale values and identifies certain features, such as the minimum value between two peaks. The histograms in this study exhibited well-defined turning points at phase transitions, as shown in Fig. 3, enabling clear thresholding of phases. Values on the left correspond to the air phase (black) and values to the right correspond

to the brine phase (white). We note that for sea ice, a distinction is sometimes made between the pore-scale microstructure of liquid veins and larger macroscopic brine drainage channels which can have diameters up to several cm. In this manuscript, we will use the term “brine channel” to refer to the entire brine phase, and since the samples studied here are relatively small (cubes measuring 7.5 mm on edge), this will primarily refer to the pore-scale microstructure of liquid veins. Since the same thresholds were to be used for all samples analyzed, the histograms of several representative samples were first examined, and average optimized values for each of the three phases were selected. These values only varied by a few greyscale values from each other and thus, each phase was clearly segmented in each sample.

3. Metrics for microstructural analysis

The data output from μ CT is both qualitative and quantitative, with each providing complementary information useful in characterizing the internal structure of the porous media. Qualitatively, software programs allow the user to visualize the full three-dimensional features of both the object and the pore structure as is shown in Fig. 4. This software enables visualization of brine channel size via color-coding as shown in the right panel of Fig. 4. Quantitatively, the user is provided with both two- and three-dimensional data that provide information regarding definition, shape, and connectivity for

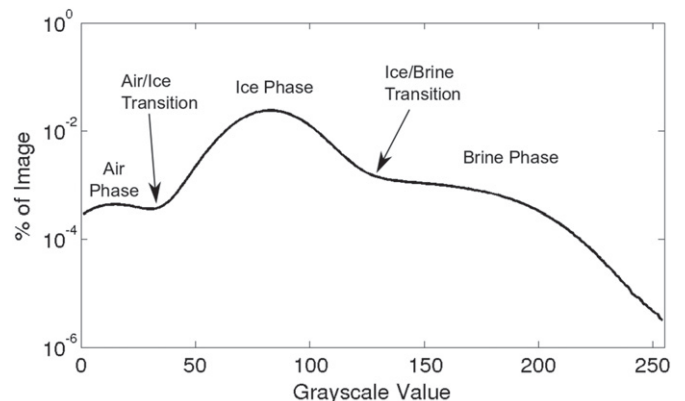


Fig. 3. Representative histogram for thresholding μ CT images. The middle peak represents the gray-scale values corresponding to the ice phase. Values on the left correspond to the air phase (black) and values to the right correspond to the brine phase (white). The turning points for the middle peak were used to set precise thresholding values. Since these values varied by only 1–3 greyscale values, an averaged value could be used for all images.

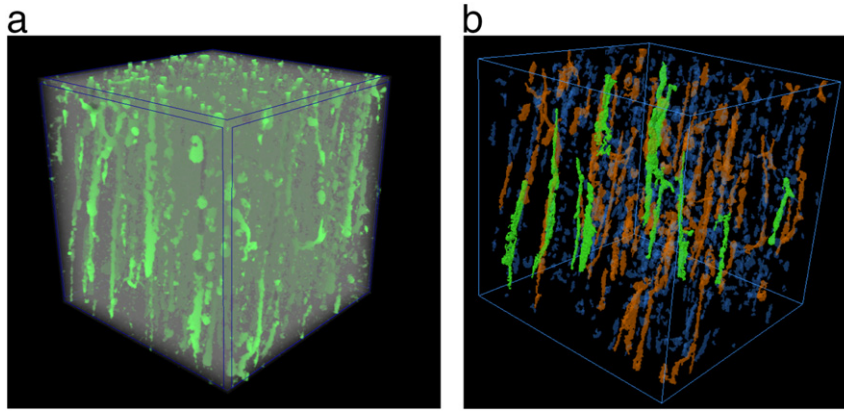


Fig. 4. Three-dimensional visualization of sea ice with brine channels of a cubic VOI measuring 7.5 mm on each edge. Left panel shows all brine channels in green. The right panel color codes brine channels by size, where channels greater than 0.0337 mm^3 are colored green, channels between 0.0067 mm^3 are colored orange, and brine channels less than 0.0067 mm^3 are blue. (For interpretation of the references to color in this figure legend, the reader is referred to the web version of this article.)

each phase. For a three-phase media such as sea ice, each phase is isolated and then analyzed separately to provide a full quantitative description of the microstructure. Prior to analysis, objects measuring less than 25 voxels, or $8.4 \times 10^{-5} \text{ mm}^3$, are discarded as noise. Then, once thresholds have been set to segment each phase, simple voxel summations provide volume, porosity, surface area, and specific surface area. Additional microstructural parameters describing convexity, morphology, anisotropy, and topology can also be determined. We note that calculations are computed on voxels, rather than smoothed curves, and thus some measurements (e.g. surface area) may be a slight over-estimate.

A variety of parameters exist to describe the shape of each phase. It should be noted, that these metrics represent the shape of the internal structures within each of these phases rather than the overall phase. We also note that when discussing a given phase below, we will use the term “object” to refer to this internal structure within the overall sample. First, the structure model index (SMI) provides a measure of surface convexity and the plate-like/rod-like architecture of a given phase. The entire surface of each object is dilated by one pixel, and the resulting surface area is calculated. SMI is defined as $\text{SMI} = 6 \left(\frac{S' \times V}{S^2} \right)$, where S' is the derivative of the change in surface area, V is the initial volume, and S^2 is the surface area prior to dilation. For benchmarks, SMI values of 4, 3, and 0, represent spheres, cylinders, and plates, respectively.

The structure thickness is an alternative metric for measuring the size of an object. To calculate the structure thickness, first the medial axes of all structures of a given phase are identified. For all voxels lying along this axis, a sphere is fitted such that the sphere is both entirely inscribed within the object and encompasses the given voxel. The structure thickness is then given as the mean diameter of all spheres over the entire volume. The structure separation is the inverse metric, providing a measurement on the spacing between individual objects. The same calculation as for structure thickness is completed, but for the non-object (i.e. pore) phase. The fractal dimension of an object quantifies how the object’s surface fills space, and provides a metric of the object’s surface complexity. It is calculated using the box counting algorithm, whereby boxes of a variety of sizes are chosen, and for each size, the number of boxes required to cover the object is counted. When the number of boxes is plotted versus box size on a log-log scale, the slope of the line yields the fractal dimension.

One final metric regarding the phase shape is the degree of anisotropy. First, the mean intercept length is calculated along a line through the three-dimensional image, and dividing the length

of the line by the number of intersections with the given phase. This process is repeated for a large number of line directions in three-dimensions. A polar plot encompassing all the mean intercept lengths is created by creating an ellipsoid with boundaries defined by the mean intercept length for each direction. Any given ellipsoid can be characterized by a matrix, and the eigenvalues for this matrix are calculated, which correspond to the lengths of the semi-major and semi-minor axes. The ratio of the largest to smallest eigenvalues then provides a metric for the degree of anisotropy, with 0 representing a perfectly isotropic object and 1 representing a completely anisotropic object.

To have a full understanding of the internal structure and of properties such as permeability, it is helpful to have an understanding of the topology and connectivity of a given phase. The Euler number $\chi(x)$ in topology provides such a metric, where $\chi(x) = \beta_0 - \beta_1 + \beta_2$ and β_0 , β_1 , and β_2 are the three Betti numbers. These define the number of objects, the connectivity, and the number of voids within objects, respectively, where the connectivity represents the number of connections that need to be severed before an object becomes disconnected (i.e. separated into two objects). The Euler number is useful in comparing connectivity of different objects as it is a topologically invariant metric. By utilizing all of these metrics for all three phases, it is possible to have a full quantitative description of the internal microstructure of sea ice using μCT .

4. Results

The brine, air, and ice phases for all sub-samples scanned were analyzed using the metrics described above. It should be noted that the phases are co-dependent, and therefore trends observed with a metric for a particular phase will be reflected in the other phases. For example, if there is a high brine volume fraction, the ice volume fraction by definition will be decreased. Thus, the following analysis focuses on a select number of metrics with a primary emphasis on the brine phase as it is the critical phase in determining sea ice microstructure. All samples were scanned at -20°C , while actual in-situ temperatures as measured in the field varied from -2°C at the ocean interface to between -14°C and -18°C at the top of the ice core. Although in-situ brine volume fractions would be greater than those measured here, the general shape and morphology of the brine network is still reflected at the colder temperature used for transport, storage, and scanning. Further work on analyzing the temperature sensitivity detected by μCT is ongoing and will be reported in a future paper.

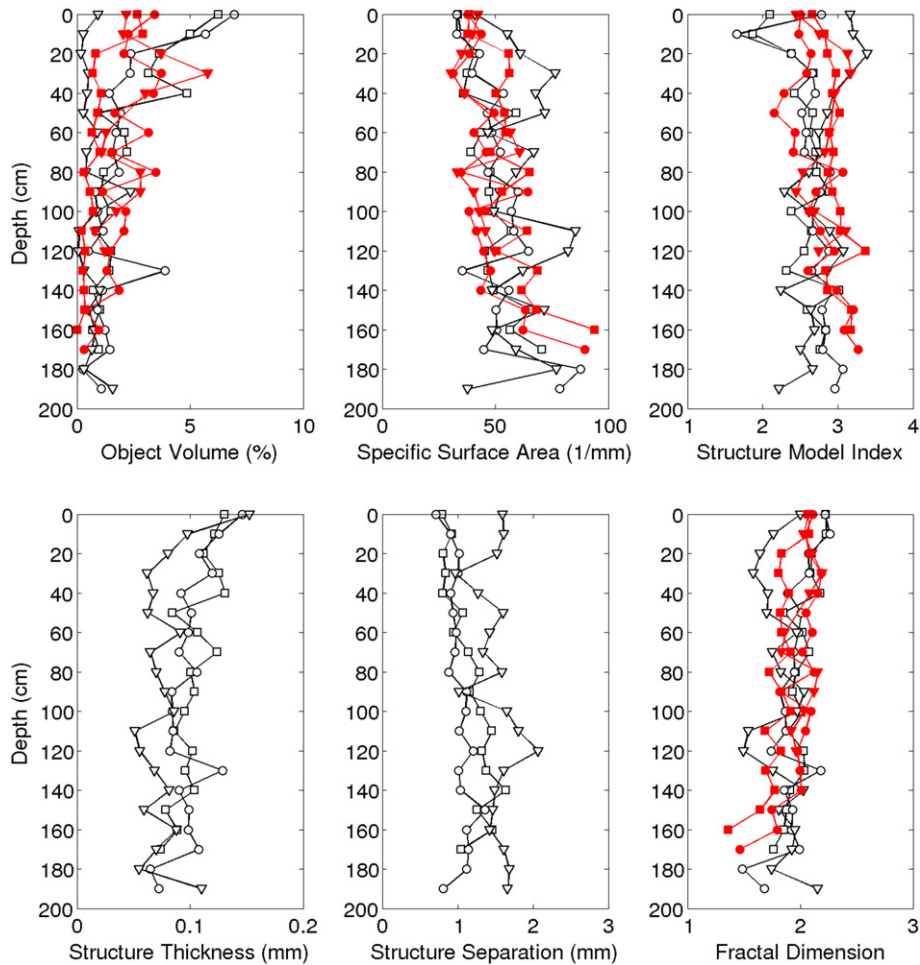


Fig. 5. μ CT metrics for analyzing the definition and shape of brine channels. The black open squares, circles, and triangles represent the Butter Point, Iceberg Site, and Scott Base cores, respectively. The red squares, circles, and triangles show the data for the three cores along the transect at distances of 6, 12, and 18 km from the ice edge, respectively. (For interpretation of the references to color in this figure legend, the reader is referred to the web version of this article.)

4.1. Brine

Figures presenting the definition and shape of the brine phase for all six cores are shown in Fig. 5. The brine volume fraction was generally less than 5%, with slightly higher fractions near the top of the core. The specific surface area increases from the top to the bottom of each core, with values relative consistent across all cores. The SMI for the brine phase was roughly 3 for all depths in all cores, indicative of a cylindrical shape, although there was more variability near the very top and bottom of each core. Structure thickness and separation were only calculated for the Butter Point, Iceberg Site, and Scott Base ice cores. For these cores, brine channels become slightly narrower deeper in the core as can be seen by a decreasing structure thickness and increasing separation with depth. The fractal dimension of the brine channels in all cores was roughly 2, suggestive of a planar geometry. This likely is an indicator that brine channels are primarily located at grain boundaries, which also have planar geometry. The degree of anisotropy for the brine channels was greatest in the middle of each core, with values relatively similar across the six cores as can be seen in the right panel of Fig. 7. The connectivity of the brine channels was quite varied, although exhibited a decreasing trend with depth as show in Fig. 6. Several of the cores had a spike in connectivity at a single depth (e.g., depth of 90 cm for the Scott Base core, depth of 50 cm for the 12 km transect core), which often corresponded with a layer of small ice grains or at the transition from frazil to columnar growth, as observed under cross-polarizing lenses.

However, when subtracted from the sum of the number of objects and cavities to yield the Euler number, the result was a relatively constant value of roughly 1000, except near the very top and bottom of the cores.

4.2. Air

For the first-year sea ice cores, the air phase represented less than 1% of the VOI and air pockets were generally cylindrical or spherical with an average SMI of slightly under 4 (Fig. 8). The multi-year ice core extracted near Scott Base had roughly an order of magnitude more air bubbles than the first-year ice cores, particularly near the top of the core. The shape of these air bubbles was also quite different, exhibiting more plate-like shapes with an average SMI of 0.8. The specific surface area of the air bubbles was similar to the brine channels, and also increased with depth in the core. The air bubble structure thickness and structure separation were relatively constant throughout the cores, with one notable exception of larger air bubbles at a depth of 50–60 cm in the Scott Base ice core. The fractal dimension of the air bubbles was also roughly two, but had more variability than did the brine channels. Like the brine channels, the air bubbles had increased degree of anisotropy in the vertical direction throughout the middle of each core, as is shown in the left panel of Fig. 7. The order of magnitude was similar to the brine channels as well, except for the Scott Base ice core where the degree of anisotropy indicated nearly purely anisotropic

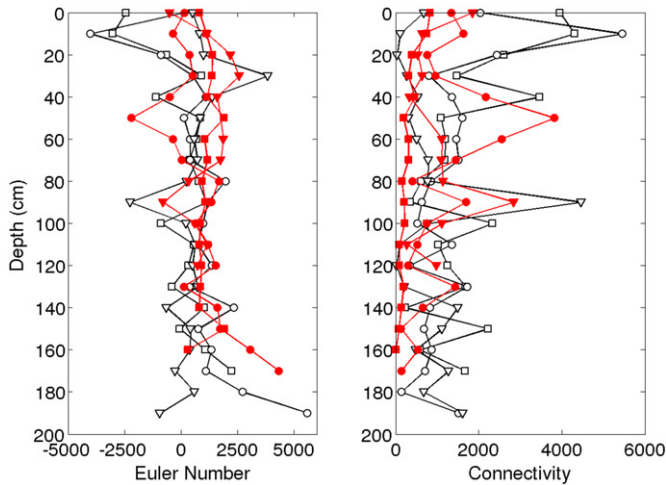


Fig. 6. The Euler number and degree of connectivity of the brine channels. The black open squares, circles, and triangles represent the Butter Point, Iceberg Site, and Scott Base cores, respectively. The red squares, circles, and triangles show the data for the three cores along the transect at distances of 6, 12, and 18 km from the ice edge, respectively. (For interpretation of the references to color in this figure legend, the reader is referred to the web version of this article.)

air bubbles, consistent with the hypothesis that these were drained brine channels.

4.3. Ice

The ice phase represents nearly the entirety of each sample, except near the top and bottom of each core. Figures illustrating the definition and shape of the ice phase are given in Fig. 9. The specific surface area was over a magnitude of order less than that of the air bubbles and brine channels. The precise values for SMI can not be compared to the reference values for objects that occupy over half the VOI, because for these large objects, the number of concavities force the SMI to become negative. However, the relative trend of decreasing SMI with depth illustrate the increased prevalence of

these concavities at deeper depths. As expected, the structure thickness of the ice phase was an order magnitude larger than for air bubbles and brine channels, with an average value of 1.0 mm. The fractal dimension of the ice phase at all depths matched the expected value of three for all cores.

4.4. Spatial variability

To assess intra-sample spatial variability, triplicate sub-samples were extracted from each depth and scanned for the Butter Point, Iceberg Site, and Scott Base cores. The percent object volume varied by less than 5% for all three phases for all sub-samples. Further, on average the specific surface area, SMI, structure thickness, structure separation, and degree of anisotropy varied by less than 5%. The fractal dimension values varied by less than 1% on all sub-samples. The only metrics with increased variability was Euler number and connectivity, which varied by approximately 15% for the brine channels. With such low measured variability, triplicate samples were not scanned for the three transect cores.

Prior to drawing conclusions from metrics obtained from μ CT, it is imperative to know the representative elementary volume (REV) for each metric. Following the methodology of Costanza-Robinson et al. (2011), we selected 13 different sized cubic VOIs, measuring 0.30, 0.60, 0.90, 1.20, 1.50, 1.88, 2.25, 2.63, 3.00, 3.75, 4.50, 6.00, and 7.50 mm on an edge. A given metric is expected to fluctuate for smaller VOIs, eventually converging upon a representative value as the VOI size reaches the REV. For each of the metrics presented above, the measured value for each phase was plotted as a function of VOI size. The resulting plots for specific surface area and structure thickness are shown in Fig. 10. As can be seen, this analysis yielded a REV for VOIs measuring 3.75 mm on an edge for both metrics for the air and brine phases. The lines representing the ice phase has mostly converged by 3.75 mm, but is truly settled by 6.0 mm. This REV was consistent with that calculated for the other metrics, and thus, it was determined that the VOI measuring 7.5 mm on edge used in this study was sufficiently large.

In addition, a single oversize scan was completed, albeit without the cooling stage due to height restrictions, for a larger rectangular prism sub-sample measuring 5 cm in height and 2 cm in width and length. Due to the larger size, the image resolution was reduced to 25 μ m. We selected 5 non-overlapping VOIs measuring the same

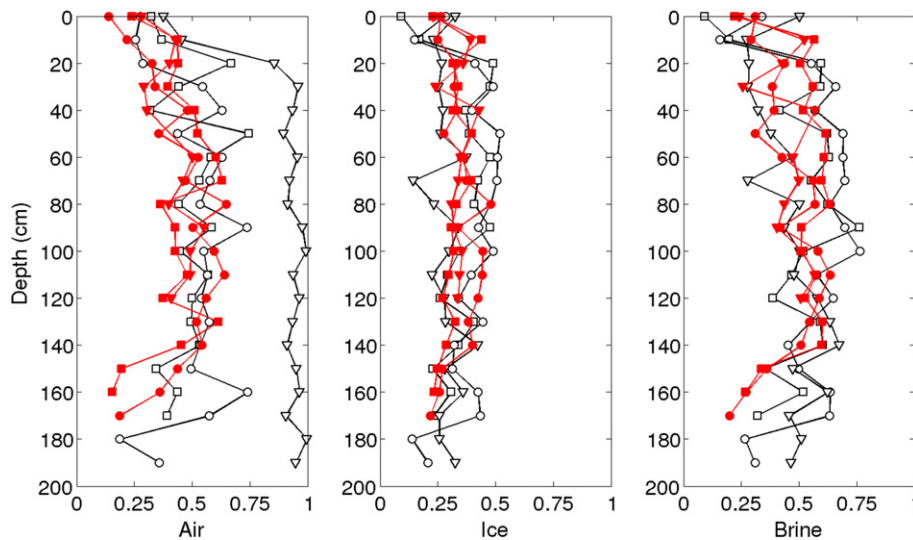


Fig. 7. The degree of anisotropy for the air, ice, and brine phases. The black open squares, circles, and triangles represent the Butter Point, Iceberg Site, and Scott Base cores, respectively. The red squares, circles, and triangles show the data for the three cores along the transect at distances of 6, 12, and 18 km from the ice edge, respectively. (For interpretation of the references to color in this figure legend, the reader is referred to the web version of this article.)

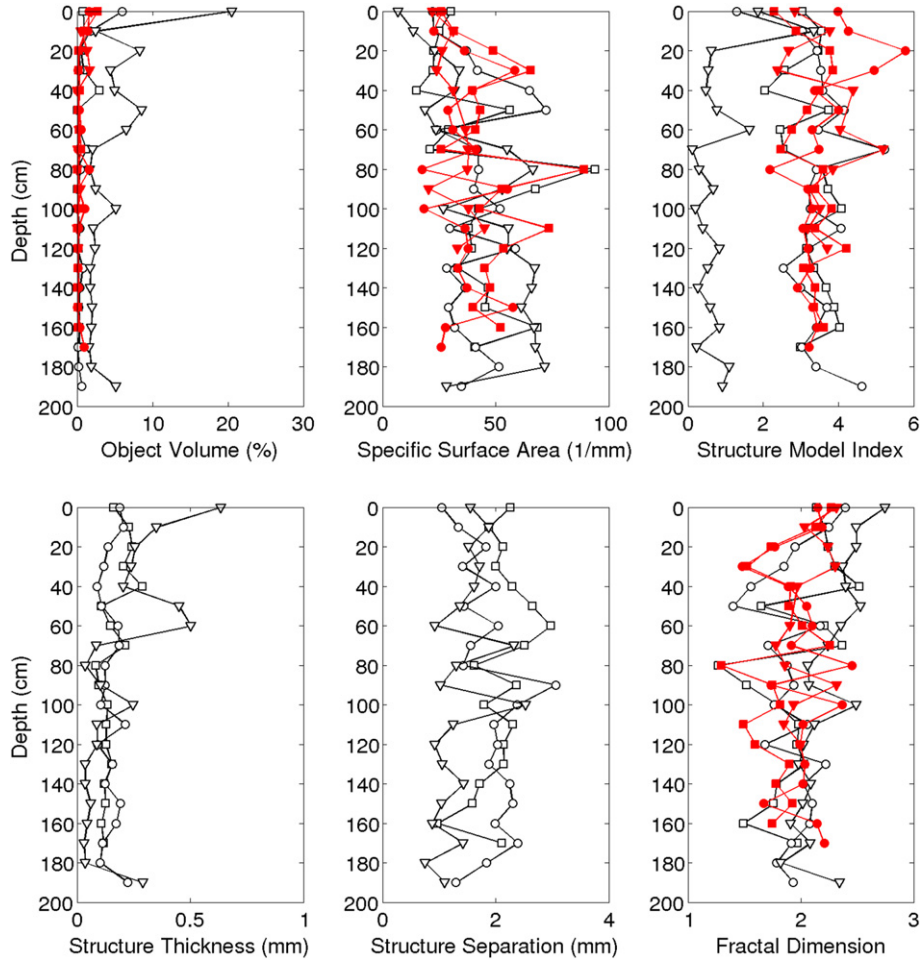


Fig. 8. μ CT metrics for analyzing the definition and shape of air pockets. The black open squares, circles, and triangles represent the Butter Point, Iceberg Site, and Scott Base cores, respectively. The red squares, circles, and triangles show the data for the three cores along the transect at distances of 6, 12, and 18 km from the ice edge, respectively. We note that for all first-year ice cores, the percent object volume of the air phase is less than 1% (top left panel). (For interpretation of the references to color in this figure legend, the reader is referred to the web version of this article.)

7.5 mm on edge from within the larger sample, and we analyzed the variability for each metric across these five VOIs. For the ice phase, the spread for most metrics was between 10%–20%, with percent object volume and fractal dimension having variability of less than 1%. The brine phase varied 10%–40%, except for fractal dimension which varied by 4%. The air phase varied the most, with most metrics varying between 30%–60%. These variations are either a result of true variability within the sample or a result of poor resolution not accurately measuring each metric. Since triplicate sampling at 15 μ m above exhibited less than 5% variability on all metrics for all three phases, we attribute the variation here to be a result of poor resolution. We also note that the air phase, which has the smallest objects, was likely most effected by the reduced resolution. The mean values across the 5 VOIs for each metric were compared to the full scan measurements also completed at 25 μ m resolution. In general, the mean value differed by less than 5% from those calculated on the entire oversized scan, except for degree of anisotropy, which differed by 10% in the air phase. Next, the mean values across the 5 VOIs were compared to the results from the nearest collected sample that was scanned at 15 μ m resolution. Here, the disparity between the two scan resolutions was quite evident. Differences were close to 50% disagreement for at least one phase on almost every metric, indicating that the reduced resolution has a significant effect on morphometric analysis.

4.5. Temperature sensitivity

Although analysis of the temperature sensitivity of measured values remains ongoing, an initial sub-sample was studied to establish a lower-bound estimate. A single sub-sample from the top of the Butter Point ice core was scanned at its in-situ temperature of -16°C and compared to the scan completed at -20°C . The brine volume fraction increased from 6.2% to 10.0% and the air volume fraction increased from 0.78% to 0.88%, and thus, the ice fraction decreased from 93.0% to 89.1%. This resulted in less than 5% change in the air phase for specific surface area, SMI, structure thickness, and connectivity. Structure separation and Euler number in the air phase changed by 24% and 36%, respectively. The brine phase specific surface area, structure thickness, and structure separation, and connectivity changed by 10%–15%, while the SMI was only affected by 4.6%. The ice phase changed by 20%–30% for specific surface area, SMI, and structure thickness, while the structure separation and connectivity changed by 10%–15%. The fractal dimensions for all phases were affected by less than 5%. The metric most affected by the change in temperature was the degree of anisotropy, which changed by 36%, 65%, and 75% for the air, ice, and brine phases, respectively. When scanned at its in-situ temperature, the air phase was more isotropic, while the ice and brine phases were more anisotropic. We do note, however, that the bottom portion of the ice core may have

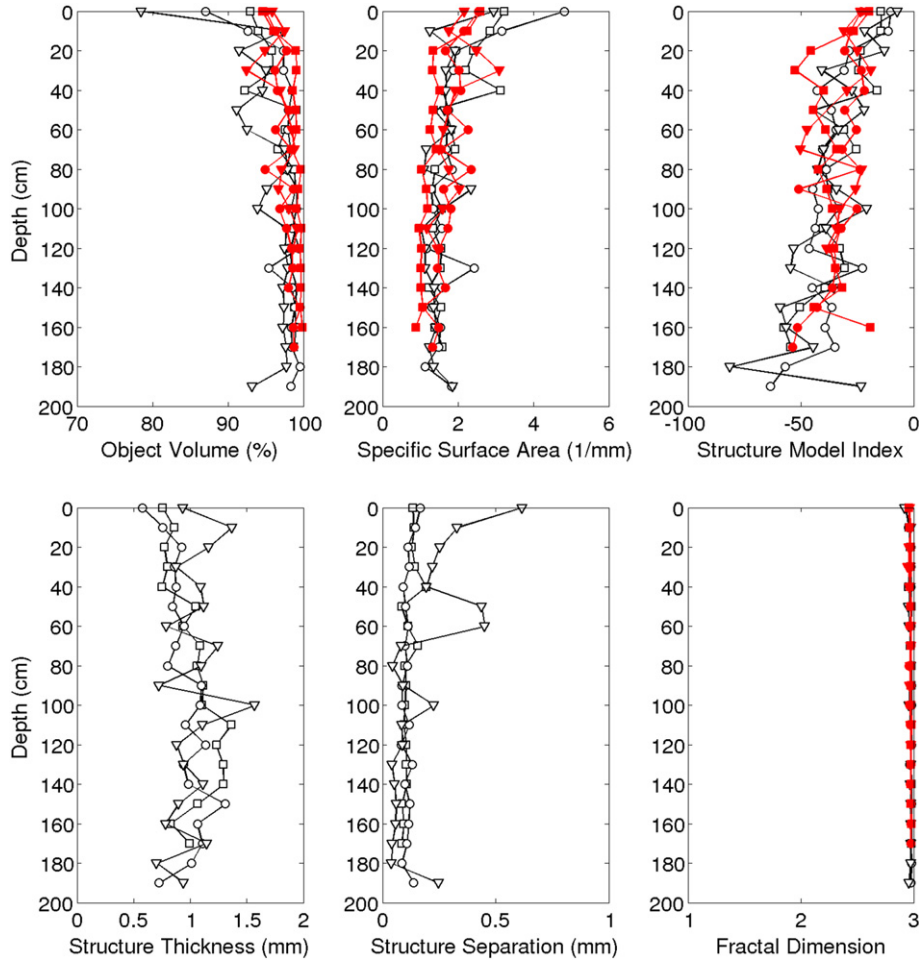


Fig. 9. μ CT metrics for analyzing the definition and shape of the ice phase. The black open squares, circles, and triangles represent the Butter Point, Iceberg Site, and Scott Base cores, respectively. The red squares, circles, and triangles show the data for the three cores along the transect at distances of 6, 12, and 18 km from the ice edge, respectively. (For interpretation of the references to color in this figure legend, the reader is referred to the web version of this article.)

experienced a larger impact from temperature changes as the in-situ temperature for the very bottom of the core is approximately -2°C . Storing and scanning at -20°C causes internal solidification, which

may irreversibly change the ice morphology. Further, this temperature change is likely to alter the air bubble fraction as the solubility of different gases causing nucleation and dissolution of gas bubbles

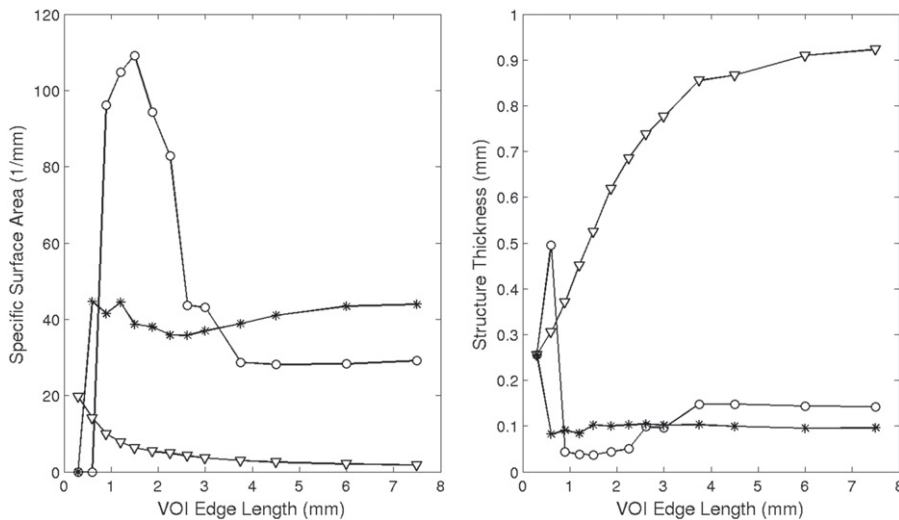


Fig. 10. Analysis for calculating the representative elementary volume (REV) for specific surface area (left) and structure thickness (right). The open circles, open triangles, and stars represent the air pockets, ice, and brine channels, respectively.

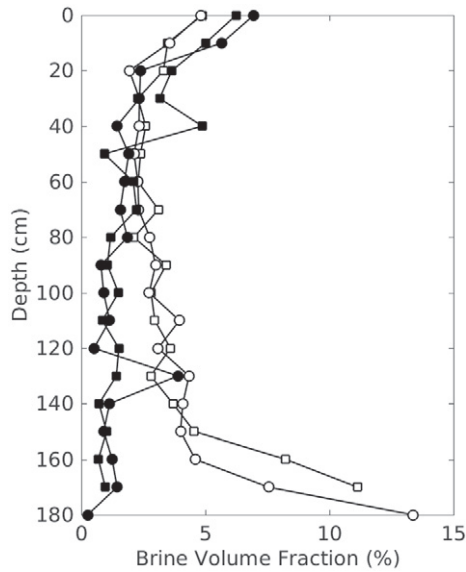


Fig. 11. Comparing μ CT-measured brine volume fraction to the expected values derived from the Frankenstein and Garner relationship (Cox and Weeks, 1983; Frankenstein and Garner, 1967). Results are shown for the Butter Point (squares) and Iceberg Site (circles) cores, where the μ CT-measured values are the filled squares and circles and the expected values are the open squares and circles.

is temperature dependent (Crabeck et al., 2016). Our following work will further address this obstacle encountered by all researchers studying sea ice cores at non-in-situ conditions.

5. Discussion

The metrics presented in this study provide a detailed microstructural description of the brine channels, air pockets, and ice of field-collected sea ice that has been cooled to a uniform temperature. Using an accelerating voltage of 40 kV with a current of 250 μ A provided an optimal balance of short acquisition time while maintaining sufficient image contrast for phase segmentation, and will be the preferred scanning parameters for future analysis. In comparison to prior μ CT analysis on laboratory-grown sea ice by Pringle et al. (2009), we have increased the spatial resolution to 15 μ m, increasing the ability to accurately define phase boundaries. Pringle et al. (2009) used targeted thresholding to matched expected values for porosity in determining phase boundaries, while the increased resolution presented here eliminates the need for prior knowledge or estimates. Additionally, the methodology developed by Obbard et al. (2009)

and used in this study does not require centrifuging samples, which eliminates the brine phase in open pores, while leaving it in closed pores.

The temperature sensitivity analysis indicated that, as expected, a four degree fluctuation did significantly alter the brine volume fraction and some of the metrics. However, many of the metrics, such as those describing the morphology of brine channels, saw a smaller degree of variation, suggesting that general shape is retained over some temperature fluctuation. Future work will include analyzing samples at in-situ temperatures to better quantify the importance of temperature. We compared the μ CT-measured brine volume fraction to expected values derived from the Frankenstein and Garner relationship relating temperature, salinity, and brine volume fraction for the Butter Point and Iceberg site core in Fig. 11 (Cox and Weeks, 1983; Frankenstein and Garner, 1967). For this analysis, we used the core temperatures and salinities presented in a companion paper to this manuscript (Lieb-Lappen and Obbard, 2015). From 0 cm to 100 cm, the measured brine volume fractions match the expected values remarkably well. However, below a depth of 100 cm in both cores, the expected brine volume fraction is much greater than what was measured using μ CT. For example, at a depth of 150 cm the expected brine volume fraction is 4.4 times greater than the values measured using μ CT, and continues to separate for lower depth samples in both cores. This provides an estimate for the degree by which the analyzed samples differed from their in-situ conditions.

The brine channels in all cores studied showed the expected vertically elongated and mostly cylindrical shape, with increasing surface area deeper in the core (Cole and Shapiro, 1998; Weissenberger et al., 1992). This is likely due to a higher degree of branching in the warmer ice, particularly in the platelet ice, at the bottom of the core. μ CT is an excellent technique to visually observe pore geometry, and specifically how brine channel structure is dependent upon ice type. In Fig. 12, we compare the brine channels at three different depths representing three different ice types in the Butter Point ice core. At 10 cm the ice is frazil ice, and the brine channels illustrate the granular texture with a high degree of isotropy. The increased variability near the top of each core for all metrics, particularly in shape as exhibited by SMI, can be attributed to this frazil ice region. The sample from 50 cm is a representative example from columnar ice, where the brine channels are generally aligned in sets of parallel layers spaced roughly at 0.5 mm, in agreement with measurements using X-ray microfluorescence in our companion paper (Obbard et al., 2016). The spacing of these layers is both consistent with the growth mechanism of sea ice (Weeks and Ackley, 1982), and with the lab-grown single crystal results of Pringle et al. (2009). The high degree of anisotropy through the middle of the core is likely a result of brine channels sandwiched between columnar ice growth. Finally, the 150-cm sample is from platelet ice, where the brine channels

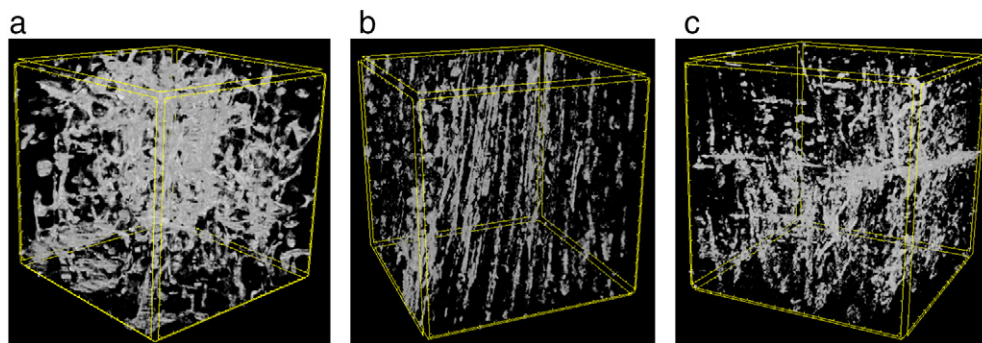


Fig. 12. Three-dimensional visualizations of the brine channels from three depths of the Butter Point ice core. The left panel is from a depth of 10cm, the middle panel is from a depth of 50cm, and the right panel is from a depth of 150cm. These correspond to representative examples of frazil ice, columnar ice, and platelet ice, respectively. Each cubic VOI measures 7.5mm on each edge.

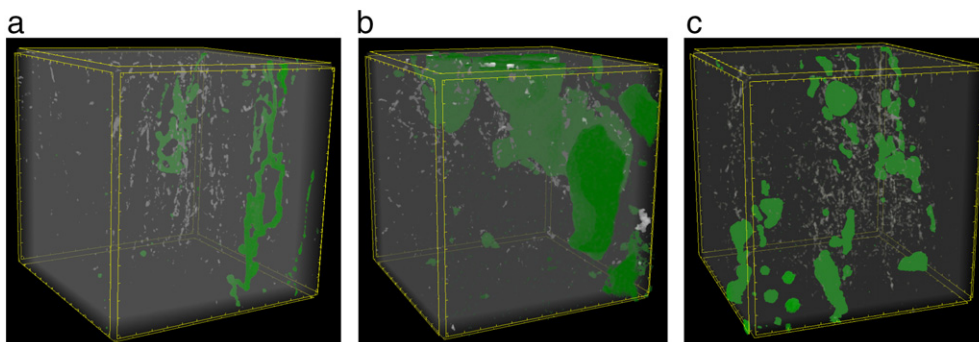


Fig. 13. Three-dimensional visualizations of air bubbles from 60 cm in the Butter Point core (left panel), 50 cm in the Scott Base core (middle panel), and 90 cm in the Scott Base core (right panel). Air bubbles are colored green in all three panels while brine channels are partially visible in white. These samples were selected to show differences between first-year ice (Butter Point core) and multi-year ice (Scott Base core). Each cubic VOI measures 7.5 mm on each edge. (For interpretation of the references to color in this figure legend, the reader is referred to the web version of this article.)

have a higher degree of lateral branching consistent with previous research (Smith et al., 2001).

Brine channel thickness was typically about 0.1 mm, which is slightly less than the 0.2–0.5 mm observed by Pringle et al. (2009). Further, the expected increase in brine channel width close to the ice-water interface (Weissenberger et al., 1992) was not observed. Both observations are likely a result of not scanning at in-situ temperatures, and consequently having a lower than expected brine volume fraction for the lower-depth samples. However, brine channel thickness was still large enough to provide sufficient habitat for bacteria (1–5 μm) and diatoms (10–200 μm), as well as pathways for nutrient delivery and transport through the interconnected pore space (Krembs et al., 2011, 2002). Since the morphological observations of this study were relatively consistent with those of Pringle et al. (2009), we would expect to observe a similar percolation threshold. We were not able to achieve scans at in-situ temperatures for this study and thus, did not calculate percolation thresholds. We also note that we did not observe any trends in brine channel morphology along the transect as all three cores were similar to the other two first-year ice cores (Butter Point and Iceberg Site).

Air pockets represented the smallest volume fraction phase and were mostly spherical in shape, except in the multi-year ice core collected at Scott Base where they were elongated in the vertical direction. This may be the result of diffusion driven by surface heating, or these features may be previous brine channels that had drained as the ice pack experienced seasonal temperature fluctuations and flushing events. Visual representations of three selected samples highlighting the differences between first-year and multi-year ice are shown in Fig. 13. For the first-year sea ice sample shown (60 cm depth in the Butter Point core), the largest air bubble clearly looks like a drained brine channel, whose shape is quite similar to brine channels in columnar ice (Fig. 12). This indicates that the pore geometry has undergone little microstructural change since the brine channel was drained. Conversely, the air bubbles in the multi-year ice core have larger diameter and are more elliptical. Through the metrics described above, we observed that there is a higher degree of anisotropy for these air bubbles relative to those found in first-year ice. This suggests that the air bubbles are remnants from several large brine drainage channels that combined during the summer melt season. Brine drainage from these pores could have occurred either during the melt season or during ice core extraction. Additionally, we note that these air bubbles are more isolated at lower depths in the ice core as can be seen in comparing the 50 cm sample (middle panel) to the 90 cm sample (right panel) in Fig. 13. Air pockets across all first-year ice cores however, were relatively consistent in volumetric size. Finally, since the ice phase represents nearly the entirety of the sample, the morphological metrics presented here are not as

insightful as for the air and brine phases. However, it was observed that the prevalence of concavities increased with depth potentially due to the increased branching of brine channels observed.

6. Conclusions

This work further established the methodology for analyzing sea ice microstructure using μCT , and presented results from six Antarctic sea ice cores stored isothermally. Metrics were developed to describe the shape, size, and topology of the different phases in sea ice. It was found that the REV for these microstructural metrics is a cube measuring 6.0 mm on each edge. Vertically oriented cylindrical brine channels were observed with increased branching at lower depths, while measurements of brine channel connectivity detected frazil/columnar transitions, as well as regions with decreased grain size. More work is needed, however, to fully understand the importance of maintaining in-situ temperature during analysis. By providing non-destructive qualitative and quantitative three-dimensional analysis, μCT is a useful tool for understanding the fine microstructure of sea ice, with potential to add critical details for use in dynamical models of sea ice.

This research was supported by a National Science Foundation (NSF) Grant # 1043145.

References

- Batenburg, K.J., Sijbers, J., 2009. Optimal threshold selection for tomogram segmentation by projection distance minimization. *IEEE T. Med. Imaging* 28 (5), 676–686.
- Baveye, P.C., Laba, M., Otten, w., Bouckaert, L., Sterpaio, P.D., Goswami, R.R., Grinev, D., Houston, A., Yaoping, Y., Liu, J., Mooney, S., Pajor, R., Sleutel, S., Tarquis, A., Wang, W., Wei, Q., Sezgin, M., 2010. Observer-dependent variability of the thresholding step in the quantitative analysis of soil images and X-ray microtomography data. *Geoderma* 157 (1), 51–63.
- Campbell, H.R.B.G.M., Klinck, R.J., MacNeil, J.A., Boyd, S.K., 2007. Automatic segmentation of cortical and trabecular compartments based on a dual threshold technique for in vivo micro-CT bone analysis. *Bone* 41 (4), 505–515.
- Cole, D.M., Shapiro, L.H., 1998. Observations of brine drainage networks and microstructure of first-year sea ice. *J. Geophys. Res.* 103 (C10), 21739–21750.
- Costanza-Robinson, M.S., Estabrook, B.D., Fouhey, D.F., 2011. Representative elementary volume estimation for porosity, moisture saturation, and air-water interfacial areas in unsaturated porous media: data quality implications. *Water Resour. Res.* 47 (7).
- Costanza-Robinson, M.S., Harrold, K.H., Lieb-Lappen, R.M., 2008. X-ray microtomography determination of air-water interfacial area-water saturation relationships in sandy porous media. *Environ. Sci. Technol.* 42 (8), 2949–2956.
- Cox, G.F.N., Weeks, W.F., 1975. Brine drainage and initial salt entrapment in sodium chloride ice. *Tech. Rep. Research Report 345*, CRREL, Hanover, NH.
- Cox, G.F.N., Weeks, W.F., 1983. Equations for determining the gas and brine volumes in sea-ice samples. *J. Glaciol.* 29 (102), 306–316.
- Crabeck, O., Galley, R., Delille, B., Else, B., Geilfus, N.-X., Lemes, M., Des Roches, M., Francus, P., Tison, J.-L., Rysgaard, S., 2016. Imaging air volume fraction in sea ice using non-destructive X-ray tomography. *Cryosphere* 10 (3), 1125–1145.

- Eicken, H., Bock, C., Wittig, R., Miller, H., Poertner, H.-O., 2000. Magnetic resonance imaging of sea-ice pore fluids: methods and thermal evolution of pore microstructure. *Cold Reg. Sci. Technol.* 31 (3), 207–225.
- Frankenstien, G., Garner, R., 1967. Equations for determining the brine volume of sea ice from -0.5°C to -22.9°C . *J. Glaciol.* 6, 943–944.
- Freitag, J., Wilhelms, F., Kipfstuhl, S., 2004. Microstructure-dependent densification of polar firn derived from X-ray microtomography. *J. Glaciol.* 50 (169), 243–250.
- Golden, K.M., Eicken, H., Heaton, A.L., Miner, J., Pringle, D.J., Zhu, J., 2007. Thermal evolution of permeability and microstructure in sea ice. *Geophys. Res. Lett.* 34 (16).
- Grannas, A.M., Jones, A.E., Dibb, J., Ammann, M., Anastasio, C., Beine, H.J., Bergin, M., Bottenheim, J., Boxe, C.S., Carver, G., Chen, G., Crawford, J.H., Domine, F., Frey, M.M., Guzman, M.I., Heard, D.E., Helmig, D., Hoffmann, M.R., Honrath, R.E., Huey, L.G., Hutterli, M., Jacobi, H.W., Klan, P., Lefer, B., McConnell, J., Plane, J., Sander, R., Savarino, J., Shepson, P.B., Simpson, W.R., Sodeau, J.R., von Glasow, R., Weller, R., Wolff, E.W., Zhu, T., 2007. An overview of snow photochemistry: evidence, mechanisms, and impacts. *Atmos. Chem. Phys.* 7, 4329–4373.
- Gregory, S.A., Albert, M.R., Baker, I., 2014. Impact of physical properties and accumulation rate on pore close-off in layered firn. *Cryosphere* 8 (1), 91–105.
- Hubbell, J.H., Seltzer, S.M., 1995. Tables of X-ray mass attenuation coefficients and mass energy-absorption coefficients 1 keV to 20 MeV for elements $z = 1$ to 92 and 48 additional substances of dosimetric interest. Tech. Rep., National Inst. of Standards and Technology-PL, Ionizing Radiation Div., Gaithersburg, MD.
- Hutchings, J.K., Heil, P., Lecomte, O., Stevens, R., Steer, A., Lieser, J.L., 2015. Comparing methods of measuring sea-ice density in the east antarctic. *Ann. Glaciol.* 56 (69), 77.
- Ketcham, R.A., Carlson, W.D., 2001. Acquisition, optimization and interpretation of X-ray computed tomographic imagery: applications to the geosciences. *Comput. Geosci.* 27 (4), 381–400.
- Krembs, C., Eicken, H., Deming, J.W., 2011. Exopolymer alteration of physical properties of sea ice and implications for ice habitability and biogeochemistry in a warmer arctic. *P. Natl. Acad. Sci.* 108 (9), 3653–3658.
- Krembs, C., Eicken, H., Junge, K., Deming, J.W., 2002. High concentrations of exopolymeric substances in arctic winter sea ice: implications for the polar ocean carbon cycle and cryoprotection of diatoms. *Deep-Sea Res.* 49 (12), 2163–2181.
- Landis, E.N., Keane, D.T., 2010. X-ray microtomography. *Mater. Charact.* 61 (12), 1305–1316.
- Lieb-Lappen, R.M., Obbard, R.W., 2015. The role of blowing snow in the activation of bromine over first-year antarctic sea ice. *Atmos. Chem. Phys.* 15 (13), 7537–7545.
- Light, B., Maykut, G.A., Grenfell, T.C., 2003. Effects of temperature on the microstructure of first-year arctic sea ice. *J. Geophys. Res.* 108 (C2).
- Maus, S., Huthwelker, T., Enzmann, F., Miedaner, M., Stampanoni, M., Marone, F., Hutterli, M.A., Hintermuller, C., Kersten, M., 2009. Synchrotron-based X-ray tomography: insights into sea ice microstructure. In: Lepparanta, M. (Ed.), *Rep. Ser. Geophys.* 61. University of Helsinki, pp. 28–45.
- Maus, S., Leisinger, S., Matzl, M., Schneebeli, M., Wiegmann, A., 2013. Modeling oil entrapment in sea ice on the basis of 3D micro-tomographic images. *Proc. Int. Conf. Port Ocean Eng. Arct. Cond.*, Vol. 22. Espoo, Finland.
- Naik, N.N., Jupe, A.C., Stock, S.R., Wilkinson, A.P., Lee, P.L., Kurtis, K.E., 2006. Sulfate attack monitored by microCT and EDXRD: influence of cement type, water-to-cement ratio, and aggregate. *Cement Concrete Res.* 36 (1), 144–159.
- Obbard, R.W., Lieb-Lappen, R.M., Nordick, K.V., Golden, E.J., Leonard, J.R., Lanzirotti, A., Newville, M.G., 2016. Synchrotron X-ray fluorescence spectroscopy of salts in natural sea ice. *Earth Space Sci.* 3, 463–479. <http://dx.doi.org/10.1002/2016EA000172>.
- Obbard, R.W., Troderman, G., Baker, I., 2009. Imaging brine and air inclusions in sea ice using micro-X-ray computed tomography. *J. Glaciol.* 55 (194), 1113–1115.
- Perovich, D.K., Gow, A.J., 1996. A quantitative description of sea ice inclusions. *J. Geophys. Res.* 101 (C8), 18327–18343.
- Pinzer, B.R., Medebach, A., Limbach, H.J., Dubois, C., Stampanoni, M., Schneebeli, M., 2012. 3D-characterization of three-phase systems using X-ray tomography: tracking the microstructural evolution in ice cream. *Soft Matter* 8 (17), 4584–4594.
- Polashenski, C., Perovich, D., Courville, Z., 2012. The mechanisms of sea ice melt pond formation and evolution. *J. Geophys. Res.* 117 (C1).
- Pringle, D.J., Miner, J.E., Eicken, H., Golden, K.M., 2009. Pore space percolation in sea ice single crystals. *J. Geophys. Res.* 114 (C12).
- Schneebeli, M., Sokratov, S.A., 2004. Tomography of temperature gradient metamorphism of snow and associated changes in heat conductivity. *Hydrol. Processes* 18 (18), 3655–3665.
- Smith, I.J., Langhorne, P., Haskell, T.G., Trodahl, H.J., Frew, R., Vennell, M.R., 2001. Platelet ice and the land-fast sea ice of McMurdo Sound, Antarctica. *Ann. Glaciol.* 33 (1), 21–27.
- Stock, S.R., 2008. Recent advances in X-ray microtomography applied to materials. *Int. Mater. Rev.* 53 (3), 129–181.
- Tarquis, A.M., Heck, R.J., Andina, D., Alvarez, A., Anton, J.M., 2009. Pore network complexity and thresholding of 3D soil images. *Ecol. Complex.* 6 (3), 230–239.
- Timco, G.W., Frederking, R.M.W., 1996. A review of sea ice density. *Cold Reg. Sci. Technol.* 24 (1), 1–6.
- Wang, X., Baker, I., 2013. Observation of the microstructural evolution of snow under uniaxial compression using X-ray computed microtomography. *J. Geophys. Res.* 118 (22), 12–371.
- Wälin, J., Leisinger, S., Klein-Paste, A., 2014. The effect of sodium chloride solution on the hardness of compacted snow. *Cold Reg. Sci. Technol.* 102, 1–7.
- Weeks, W.F., Ackley, S.F., 1982. The growth, structure, and properties of sea ice. *Tech. Rep.*, CRREL, Hanover, NH.
- Weissenberger, J., Dieckmann, G., Gradinger, R., Spindler, M., 1992. Sea ice: a cast technique to examine and analyze brine pockets and channel structure. *Limnol. and Oceanogr.* 37 (1), 179–183.